which considered the intrinsic radioactivity of ^{176}Lu (Watson *et al* 2004). In addition, we visually compared the reconstructed image and profile of an annulus phantom with the experimental image. The sinogram projections which included scatter obtained from a view of the direct sinogram were also compared. The phantom was a water-filled cylinder with both a length and diameter of 20 cm each, and included a smaller tube 20 cm in length with an outer diameter of 6 cm and inner diameter of 5 cm filled with ^{18}F solution located at a cylinder radius of 5 cm. The experimental image was acquired by an emission scan of 20 min with 185 MBq ^{18}F solution in the tube after a transmission of 20 min using three ^{68}Ga/^{68}Ge sources.

The simulation images were obtained using the following procedures. Two gamma rays (511 keV) with back-to-back angular distributions were radiated on the target phantom. In order to reduce computation time we did not simulate transportation of positrons. We took into account the following electromagnetic processes: Compton scatter, photoelectric effect, Rayleigh scatter, multiple scatter, bremsstrahlung, and ionization. The first three processes involve gamma rays, while the rest involve electrons. Positions where gamma rays interacted with the scintillator and deposited their energy were stored in (x, y, z) coordinates in the list mode. We did not blur the interacting points. The energy resolution was set to 15% (FWHM). The value was experimentally determined from energy spectra of the whole detector system by counting the number of single events for each energy window set to 195–205, 205–215, ... and 695–705 keV. We then created a 3D sinogram in the ECAT 3D format. Finally, we reconstructed the image into a 128 $\times$ 128 matrix and 47 slices by Fourier rebinning and filtered backprojection (FBP) with attenuation correction and scatter correction based on the single scatter simulation (Watson *et al* 1995, Ollinger 1996, Watson *et al* 1997). The image reconstruction including these corrections was performed by the PET software (ECAT 7.2: Siemens). The attenuation map was calculated analytically from the tissue data. The normalization was also performed analytically. In the normalization we did not correct for the fluctuation of detector gains because of the uniform gains in the simulation.

2.5. Simulation of a cardiac PET examination using ^{15}O-water

We investigated the effects of scatter on the simulation's quantification of MBF and PTF. We assigned activities to the myocardium, cardiac cavities, liver, and lung of the numerical human model and created 3D sinograms of each area. For each area 3 $\times$ 10^9 pairs of gamma rays were assessed. We then combined the sinograms at a ratio of organ activity that was estimated based on an experimental time activity curve (TAC) (Bq/mL) obtained from a clinical cardiac examination and the organ volumes (mL) of the numerical human model (myocardium: 410 mL; liver: 1161 mL; lung: 3341 mL; cardiac cavities: 480 mL) under the assumption that the activity of each organ was homogeneous. The clinical examination was performed with a patient (male, age 57 yr) using ECAT ACCEL and ^{15}O-water; images were reconstructed into 38 frames (5 s $\times$ 24, 15 s $\times$ 8, 30 s $\times$ 6) by FBP with attenuation and scatter corrections. The protocol was approved by the local ethics committee of the National Cerebral and Cardiovascular Center.

To construct the experimental TAC, regions of interest (ROIs) were carefully drawn at the centers of organs to avoid spillover. With respect to the myocardium, it is difficult to remove spillover so we estimated the TAC using the equation $C(t) = \mathrm{PTF} \cdot \mathrm{MBF} \cdot a(t) \otimes \exp(-\mathrm{MBF} \cdot t/p)$ for a conventional single-tissue compartment model (Kety 1951, 1960) assumed to have 1.0 mL/min/g of MBF and 1.0 g mL^{-1} of PTF ($C(t)$ = TAC of myocardium, $a(t)$ = experimental input function, $p = 0.91$ for water partition coefficient, and t = time). We converted the combined sinogram to the ECAT 3D format, and reconstructed the following

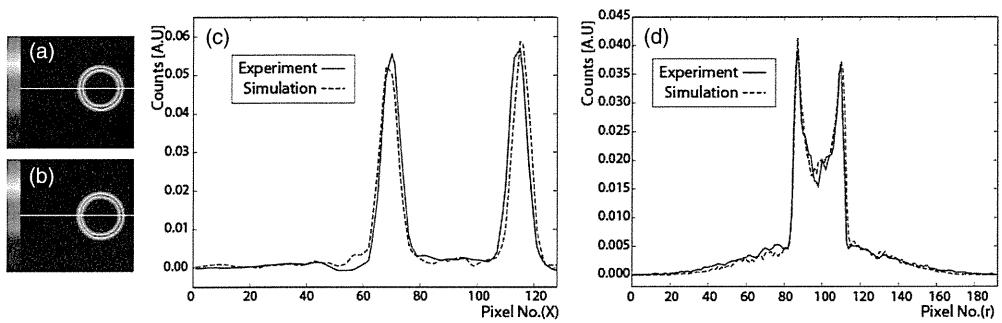

Figure 2. (a) and (b) show reconstruction images of the phantom of a simplified myocardium obtained from the experiment and the simulation, respectively. (c) Profiles at the levels of the white lines in (a) and (b), normalized by total counts. (d) Sinogram projections normalized by total counts obtained from the experiment and the simulation. These projections were taken from a view of the direct sinogram.

four image types using the FBP method without any smoothing filters: scatter-corrected image (SC), scatter-uncorrected image (W/O SC), attenuation-uncorrected image (W/O AC), and true image (TRUE). TRUE, which cannot be obtained experimentally, was reconstructed using a sinogram in which scatter was eliminated completely. For this type of image, scatter correction was not carried out, but correction was made for gamma ray attenuation. We compared SC with TRUE to evaluate the accuracy of the scatter correction implemented by the PET software. If the scatter correction was sufficiently accurate, SC would be equivalent to TRUE. We created 76 3D sinograms (38 frames for TRUE and 38 frames for SC, W/O AC and W/O SC) and reconstructed them into simulation images with different organ ratios (e.g., myocardium : liver : lung : ventricles = 1 : 0.4 : 4.5 : 3.1 at the 15th frame) according to the TAC in figure 3. The reconstructed images were scaled, where the ROI value of the cavity of the left ventricle (LV) in the SC at the 15th frame corresponded to that of the experimental value. Finally, we calculated regional MBFs and PTFs with a single-tissue compartment model, including spillover correction for the left and right ventricles (Iida *et al* 1992, Hermansen *et al* 1998, Katoh *et al* 2004), for the four types of images. MBFs and PTFs were represented in 17-segment polar maps together with polar maps normalized by the values of TRUE, called true MBF and true PTF, respectively. In this simulation, neither cardiac nor respiratory motion was generated. A motionless heart and minimized spillover from the myocardium allowed us to use a TAC with LV as the input function.

Three billion pairs of gamma rays were propagated in each organ. The simulation was performed in parallel using five personal computers with comparable specifications (Linux operating system installed on a 2.4 GHz Intel Core 2 Quad with 2 GB of memory) and twenty processors. These computations took about 60 h to complete.

3. Results

3.1. Scatter fractions and phantom images

In order to check the adequacy of the simulation, we compared the scatter fractions and images of an annulus phantom obtained in both the experiment and the simulation. The scatter fractions in the experiment and the simulation were 45.0% and 45.9%, respectively. These values also agreed with the value (46.5%) obtained in another study (Herzog *et al* 2004) using the NEMA NU2–2001 standard. Figures 2(a) and (b) show images of the annulus phantom

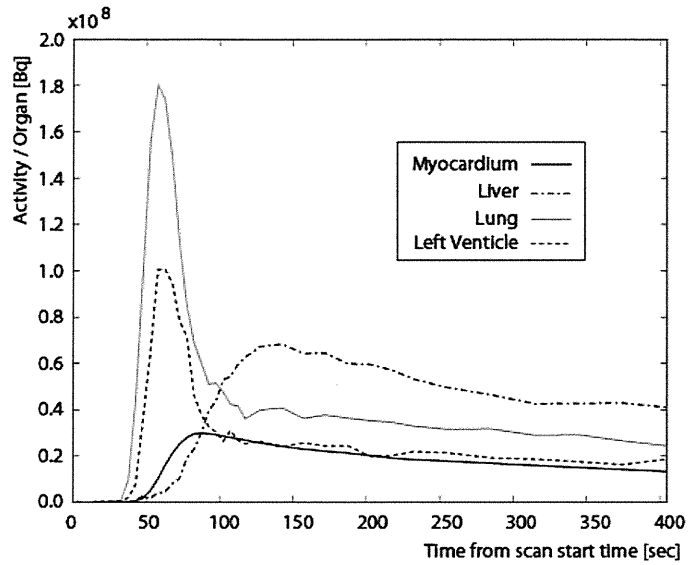

Figure 3. Activities in whole organs as functions of time. Activities were estimated from an experimental TAC (Bq/mL) and used organ volumes (mL) from the numerical human model (myocardium: 410 mL; liver: 1161 mL; lung: 3341 mL; cardiac pool: 480 mL).

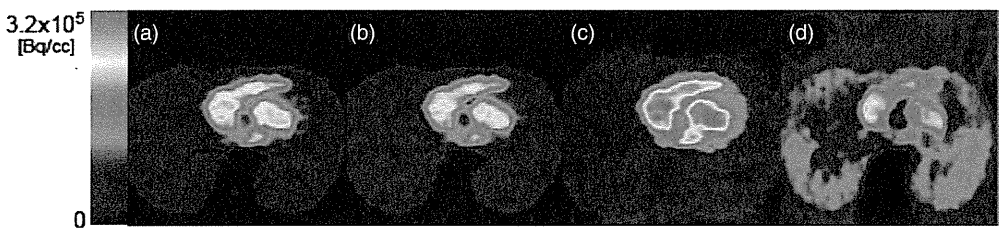

Figure 4. Representative simulation images at the center of the FOV (at the 15th frame). (a) Scatter-corrected image (SC). (b) True image (TRUE). (c) Scatter-uncorrected image (W/O SC). (d) Attenuation-uncorrected image (W/O AC) scaled by a factor of 10.

with activity in the tube from the experiment and the simulation, respectively. Figure 2(c) shows the profiles of the images at the levels of the white lines in figures 2(a) and (b), which were normalized by total counts. Figure 2(d) shows sinogram projections normalized by total counts obtained from the experiment and the simulation. The simulation image was visually consistent with the experimental image, and the profile had consistency. The ratio of peak to baseline counts in the simulation reproduced the experimental ratio within 6%. The simulation projection was also consistent with the experimental projections.

3.2. Quantification of MBF and PTF

The TAC (Bq) of each organ estimated from the clinical TAC (Bq/mL) and organ volumes (mL) of the numerical human model are shown in figure 3. Though the activity concentration of the lung was low, the activity of the whole lung was large due to its large volume, especially in the early phase. At 140 s from the scan start time, the portion of the liver adjacent to the heart had an activity approximately 2.5 times larger than that of the myocardium. Representative simulation images at the 15th frame (70 s from the scan start time) are shown in figure 4. TRUE

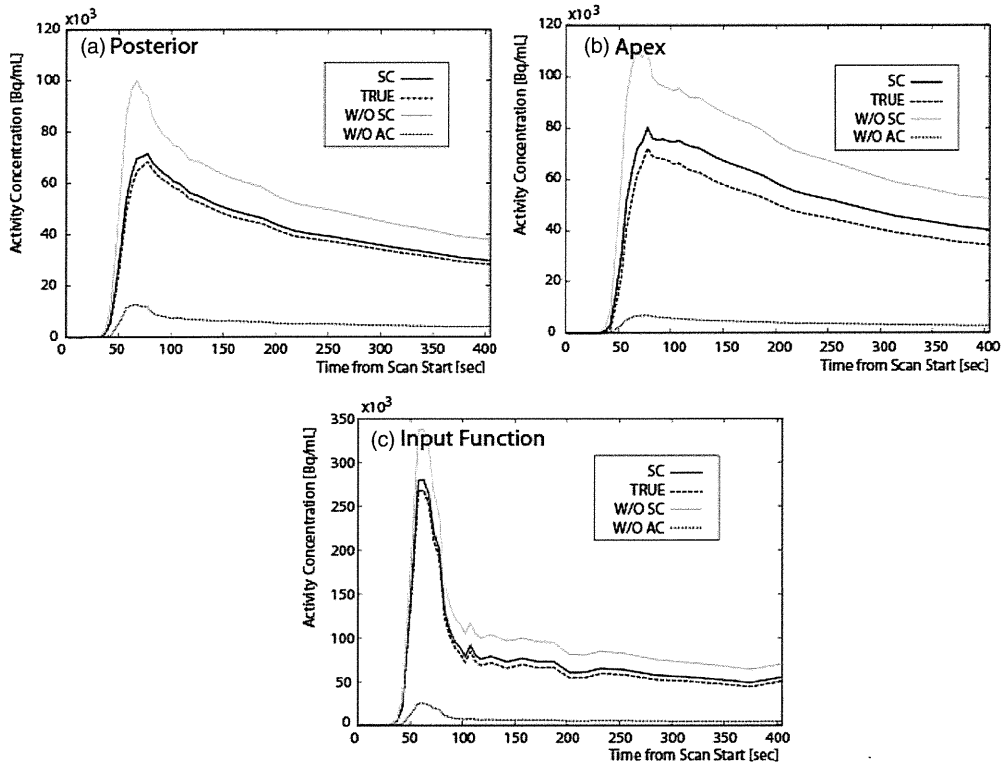

Figure 5. (a) TAC of posterior myocardium, (b) TAC of apex myocardium, (c) input function (TAC of left ventricle cavity obtained from the simulation for each type of image). Abbreviations; SC, TRUE, W/O SC and W/O AC stand for scatter-corrected image, true image, scatter-uncorrected image, and attenuation-uncorrected image, respectively.

was sharply defined because scatter was fully eliminated, while other images were relatively blurred. The SC image however was almost equivalent to TRUE image. An input function (TAC of the LV) and TAC of posterior and apex myocardium are shown in figure 5. The TAC derived from the SC corresponded to that derived from TRUE both in the input function and the posterior myocardium, and even higher activity existed in the portions of the liver and lung located partially outside the FOV. This tendency was observed for other areas of the myocardium except for the apex, for which the TAC was overestimated by approximately 15%. Polar maps of MBF calculated from dynamic simulation images are shown in figures 6(a)–(d), while normalized maps based on the true MBF are depicted in figures 6(e)–(g). Polar maps of PTF and the normalized maps are shown in figure 7. Means $\pm$ SD of normalized MBFs of SC, W/O AC, and W/O SC were 1.03 $\pm$ 0.05, 1.08 $\pm$ 0.18, and 1.13 $\pm$ 0.08, respectively. As for the normalized PTF, means of SC, W/O AC, and W/O SC were 1.00 $\pm$ 0.07, 1.35 $\pm$ 0.50 and 0.85 $\pm$ 0.09, respectively. Although equivalent MBFs within about 10% were obtained from all types of images, only the PTF of SC was close in value to the true PTF.

4. Discussion

4.1. Adequacy of the simulation

The scatter fraction obtained in the simulation was in good agreement with the experimental value. Scatter reproducibility is essential for our simulation in order to accurately estimate

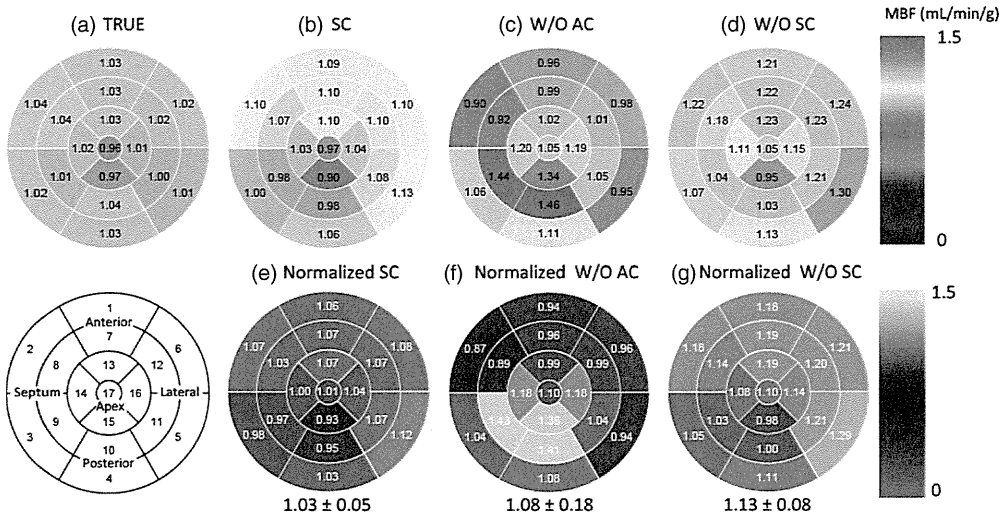

Figure 6. (a)–(d) Polar maps of absolute MBF. (e)–(g) Polar maps of MBFs normalized by the true MBF. The means ± SDs of normalized MBFs were 1.03 ± 0.05, 1.08 ± 0.18 and 1.13 ± 0.08 for SC, W/O AC, and W/O SC, respectively. Legend abbreviations are the same as in figure 5.

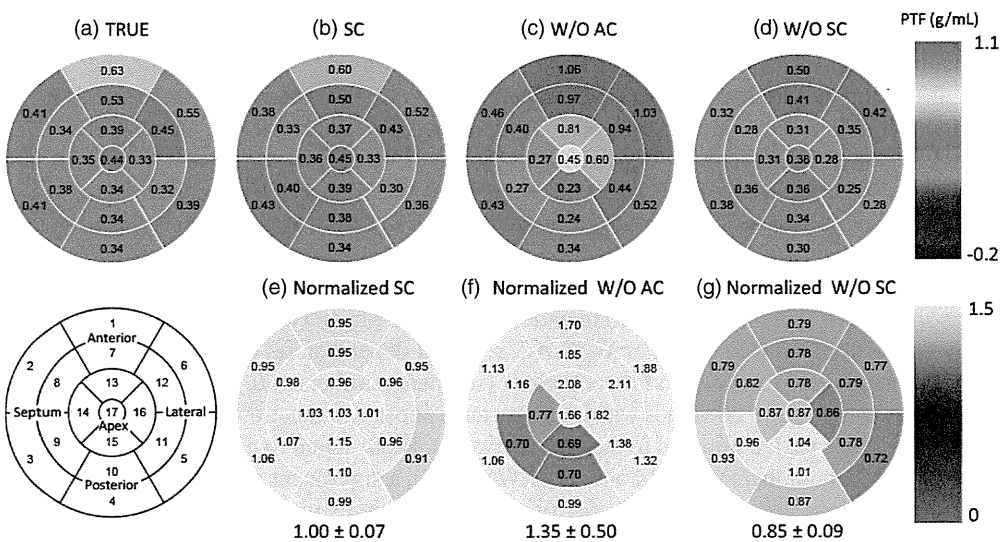

Figure 7. (a)–(d) Polar maps of absolute PTF. (e)–(g) Polar maps of PTF normalized by the true PTF. The means ± SDs of normalized PTFs were 1.00 ± 0.07, 1.35 ± 0.50 and 0.85 ± 0.09 for SC, W/O AC, and W/O SC, respectively. Legend abbreviations are the same as in figure 5.

the influence of scatter on quantitative MBF and PTF, the values of which this simulation determined with good accuracy. Furthermore, the simulation image of the phantom and profiles were also consistent with the experimental data. In these profiles, tails of peaks were small, which indicated that scatter was corrected accurately in both the simulation and the experiment. The sinogram projections also had consistency. Differing from the profiles of the images, scatter was still not corrected, resulting in tails of the peaks being observed.

The simulation is therefore appropriate in fulfilling the purpose of this study, and should be a reliable tool for estimation of scatter in 3D-PET.

4.2. Effects of scatter on MBF and PTF

TAC of the SC coincided with that of TRUE, indicating that scatter was accurately corrected. For the myocardial apex, the TAC of the SC was overestimated (15%) and was relatively larger than for other myocardium regions. This was likely due to uncorrected scatter originating from the liver bordered by the apex, because a similar simulation that excluded the activities of liver and lung demonstrated less overestimation. Absolute TAC without corrections naturally was much different from true TAC. The TAC of W/O AC was much smaller, because arms of the numerical human model beside the body caused strong absorption. However, absolute MBFs derived from not only SC but also W/O SC and W/O AC were in agreement with MBFs of TRUE regardless of the differences between absolute TAC. This is because MBF was calculated from the washout rate of the tracer, and the washout rates for all types of images were similar. This simulation showed that scatter and absorption did not change the shape of the TAC in the clearance phase. Our finding that MBFs derived from W/O AC and SC were equivalent was consistent with the results of Lubberink *et al* (2010), which were observed in a clinical context. However, in our simulation, MBF of the septum and posterior myocardium (segment numbers 9 and 10 of W/O AC in figure 6) was overestimated by about 40%. This was because spillover originated from lung activity, and the lung was located close to the myocardium in the numerical human model. In a similar simulation that did not include lung activity, the overestimation was reduced to almost zero. As this simulation has indicated, scatter and absorption have a small effect on the clearance rate of ^{15}O-water, and variation of absolute MBF of almost segment is suppressed within about 10% even without attenuation and scatter corrections. This is one of the advantages of ^{15}O-water in such scans.

In contrast to MBF, scatter correction is clearly essential for accurate PTF measurement. Although PTF derived from SC had good agreement with TRUE, PTF was overestimated by 35% for W/O AC and underestimated by 15% for W/O SC. For W/O SC, due to scatter effects we observed a relatively large overestimation in the input function rather than the tissue TAC $C(t)$, as shown in figure 5. This resulted in underestimation of the PTF value because PTF was roughly proportional to $C(t)/a(t)$. For W/O AC, regional dependencies of errors on PTF values were observed. From anterior to lateral regions (segment numbers 1, 6, 7, 12 and 13 of W/O AC), overestimation of PTF values was found because photon attenuation was smaller in the myocardial regions, $C(t)$, compared to the LV cavity, $a(t)$. From septal to posterior regions near the apex (segment numbers 9, 10, 14 and 15 of W/O AC), a significant attenuation effect in the myocardial regions rather than the LV cavity resulted in underestimation of PTF values.

PTF or perfusable tissue index (PTI) defined by PTF/ATF (anatomic tissue fraction) is useful as a marker of myocardial viability (Knaapen *et al* 2003), and several studies on the relationship between PTI and myocardial viability have been made (Yamamoto *et al* 1992, de Silva *et al* 1992, Gerber *et al* 1998, Itoh *et al* 2002). PTI can also be potentially used to noninvasively assess myocardial fibrosis (Knaapen *et al* 2004). Use of a ^{15}O-water scan sequential to a ^{15}O-CO scan could provide not only quantitative MBF but also PTI, which would also be the advantage of ^{15}O cardiac PET. The ^{15}O-CO scan, together with a transmission scan, is needed for calculation of ATF; however a single low-dose CT scan could provide ATF and serve as a substitute for these scans, resulting in reduction of scan duration, radiation dose, and risk of patient motion between scans (Harms *et al* 2011).

In the simulation, spillover was minimized because gamma ray detection points could be identified absolutely and the heart was motionless. Nevertheless, some spillover was still

observed due to the binning and interpolation involved in creating sinograms and image reconstruction, which caused about 0.3 of arterial blood volume. This simulation did not include other causes of spillover such as limited spatial resolution, positron range, cardiac motion, etc. However, even if these were included, current results would be considered valid because scatter distribution and the myocardium image would only be blurred.

The methodology developed in this work can be applied to other tracers to estimate the effects of scatter on absolute MBF. In addition, we can investigate the influence of positron range and cardiac motion on spillover and quantification of MBF. Geant4 enables propagation of positrons, and the XCAT phantom (Segars *et al* 2010) that provides the possibility of cardiac motion.

5. Conclusion

We investigated the effects of scatter on quantitative myocardium blood flow (MBF) and perfusable tissue fraction (PTF) using a precise three-dimensional positron emission tomography (3D-PET) simulation with a numerical human model. The simulation had good agreement with the experimental scatter fraction and a phantom image. In this simulation of a cardiac 3D-PET scan, scatter was corrected accurately for every region of the myocardium, and absolute MBFs remained unchanged even when the scatter and attenuation corrections were not applied. This simulation demonstrated that quantification of MBF using 3D-PET and ^{15}O-water was less affected by scatter and absorption. In contrast, to obtain accurate PTF, scatter correction was necessary.

Acknowledgments

This research was partially supported by a 2009 Grant-in-Aid for Young Scientists (B), no 21791237, from the Ministry of Education, Culture, Sports, Science and Technology of Japan.

References

Agostinelli S *et al* 2003 GEANT4 a simulation toolkit *Nucl. Instrum. Methods Phys. Res.* A **506** 250–303

Akkurt H and Echerman F K 2007 Development of PIMAL: mathematical phantom with moving arms and legs *Oak Ridge National Laboratory Report* ORNL/TM-2007/14

Brink I, Schumacher T, Talazko J, Reuland P, Mix M, Schindler T, Moser E A and Nitzsche E U 1991 3D-cardiac-PET: a recommendable clinical alternative to 2D-cardiac-PET? *Clin. Positron Imaging* **2** 191–6

Cherry S R, Woods R P, Hoffman E J and Mazziotta J C 1993 Improved detection of focal cerebral blood flow changes using three-dimensional positron emission tomography *J. Cereb. Blood Flow Metab.* **13** 630–8

deKemp R A, Yoshinaga K and Beanlands R S 2007 Will 3-dimensional PET-CT enable the routine quantification of myocardial blood flow? *J. Nucl. Cardiol.* **14** 380–97

de Silva R, Yamamoto Y, Rhodes C G, Iida H, Nihoyannopoulos P, Davies G J, Lammertsma A A, Jones T and Maseri A 1992 Preoperative prediction of the outcome of coronary revascularization using positron emission tomography *Circulation* **86** 1738–42

Gerber B L, Melin J A, Bol A, Labar D, Cogneau M, Michel C and Vanoverschelde J L 1998 Nitrogen-13-ammonia and oxygen-15-water estimates of absolute myocardial perfusion in left ventricular ischemic dysfunction *J. Nucl. Med.* **39** 1655–62

Harms H J, de Haan S, Knaapen P, Allaart C P, Lammertsma A A and Lubberink M 2011 Parametric images of myocardial viability using a single 15O-H2O PET/CT scan *J. Nucl. Med.* **52** 745–9

Hermansen F, Rosen S D, Fath-Ordoubadi F, Kooner J S, Clark J C, Camici P G and Lammertsma A A 1998 Measurement of myocardial blood flow with oxygen-15 labelled water: comparison of different administration protocols *Eur. J. Nucl. Med.* **25** 751–9

Herzog H, Tellmann L, Hocke C, Pietrzyk U, Casey M E and Kuwrt T 2004 NEMA NU2–2001 guided performance evaluation of four Siemens ECAT PET scanners *IEEE Trans. Nucl. Sci.* **51** 2662–9

Hirano Y, Koshino K and Iida H 2010 A Monte Carlo estimation of effects of activity outside field of view in O-15 cardiac 3D-PET *IEEE Med. Imaging Conf. Rec.* 2535–8

Ibaraki M, Miura S, Shimosegawa E, Sugawara S, Mizuta T, Ishikawa A and Amano M 2008 Quantification of cerebral blood flow and oxygen metabolism with 3-dimensional PET and 15O: validation by comparison with 2-dimensional PET *J. Nucl. Med.* **49** 50–9

Iida H, Rhodes C G, de Silva R, Araujo L I, Bloomfield P M, Lammertsma A A and Jones T 1992 Use of the left ventricular time-activity curve as a noninvasive input function in dynamic oxygen-15-water positron emission tomography *J. Nucl. Med.* **33** 1669–77 (available at http://jnm.snmjournals.org/content/33/9/1669.short)

Itoh H *et al* 2002 Perfusable tissue index obtained by positron emission tomography as a marker of myocardial viability in patients with ischemic ventricular dysfunction *Circ. J.* **66** 341–4

Katoh C, Morita K, Shiga T, Kubo N, Nakada K and Tamaki N 2004 Improvement of algorithm for quantification of regional myocardial blood flow using ^{15}O-water with PET *J. Nucl. Med.* **45** 1908–16 (available at http://jnm.snmjournals.org/content/45/11/1908.short)

Kety S S 1951 The theory and applications of exchange of inert gas at the lungs and tissues *Pharmacol. Rev.* **3** 1–41

Kety S S 1960 Measurement of local blood flow by the exchange of an inert diffusible substance *Methods Med. Res.* **8** 228–36

Knaapen P, Boellaard R, Götte M J, Dijkmans P A, van Campen L M, de Cock C C, Luurtsema G, Visser C A, Lammertsma A A and Visser F C 2004 Perfusable tissue index as a potential marker of fibrosis in patients with idiopathic dilated cardiomyopathy *J. Nucl. Med.* **45** 1299–304 (available at http://jnm.snmjournals.org/content/45/8/1299.short)

Knaapen P, Boellaard R, Götte M J, van der Weerdt A P, Visser C A, Lammertsma A A and Visser F C 2003 The perfusable tissue index: a marker of myocardial viability *J. Nucl. Cardiol.* **10** 684–91

Knaapen P *et al* 2010 Cardiac PET/CT: advanced hybrid imaging for the detection of coronary artery disease *Neth. Heart J.* **18** 90–8

Knesaurek K, Machac J, Krynyckyi B R and Almeida O D 2003 Comparison of 2-dimensional and 3-dimensional 82Rb myocardial perfusion PET imaging *J. Nucl. Med.* **44** 1350–6 (available at http://jnm.snmjournals.org/content/44/8/1350.short)

Knuuti J, Kajander S, Mäki M and Ukkonen H 2009 Quantification of myocardial blood flow will reform the detection of CAD *J. Nucl. Cardiol.* **6** 497–506

Lodge M A, Badawi R D, Gilbert R, Dibos P E and Line B R 2006 Comparison of 2-dimensional and 3-dimensional acquisition for 18F-FDG PET oncology studies performed on an LSO-based scanner *J. Nucl. Med.* **47** 23–31 (available at http://jnm.snmjournals.org/content/47/1/23.short)

Lubberink M, Boellaard R, van der Weerdt A P, Visser F C and Lammertsma A A 2004 Quantitative comparison of analytic and iterative reconstruction methods in 2- and 3-dimensional dynamic cardiac 18F-FDG PET *J. Nucl. Med.* **45** 2008–15 (available at http://jnm.snmjournals.org/content/45/12/2008.short)

Lubberink M, Harms H J, Halbmeijer R, de Haan S, Knaapen P and Lammertsma A A 2010 Low-dose quantitative myocardial blood flow imaging using 15O-water and PET without attenuation correction *J. Nucl. Med.* **51** 575–80

Moreno-Cantu J J, Thompson C J and Zatorre R J 1998 Evaluation of the ECAT EXACT HR1 3-D PET scanner in H2O-15 brain activation studies: dose fractionation strategies for rCBF and signal enhancing protocols *IEEE Trans. Med. Imaging* **17** 979–85

Nagaoka T, Watanabe S, Sakurai K, Kunieda E, Watanabe S, Taki M and Yamanaka Y 2004 Development of realistic high-resolution whole-body voxel models of Japanese adult male and female of average height and weight, and application of models to radio-frequency electromagnetic-field dosmietry *Phys. Med. Biol.* **49** 1–15

Ollinger J M 1996 Model-based scatter correction for fully 3D PET *Phys. Med. Biol.* **41** 153–176

Roelants V, Bol A, Bernard X, Coppens A, Melin J, Gerber B and Vanoverschelde J L 2006 Direct comparison between 2-dimensional and 3-dimensional PET acquisition modes for myocardial blood flow absolute quantification with O-15 water and N-13 ammonia *J. Nucl. Cardiol.* **13** 220–4 (available at http://www.onlinejnc.com/journal/12350/13/2/BF02971246_10.1007_BF02971246/2008/Direct_comparison_between_2-dimensional_and_3-dime.html)

Sadato N, Carson R E, Daube-Witherspoon M E, Campbell G, Hallett M and Herscovitch P 1997 Optimization of noninvasive activation studies with 15O-water and three-dimensional positron emission tomography *J. Cereb. Blood Flow Metab.* **17** 732–9

Schäfers K P, Spinks T J, Camici P G, Bloomfield P M, Rhodes C G, Law M P, Baker C S and Rimoldi O 2002 Absolute quantification of myocardial blood flow with H2 15O and 3-dimensional PET: an experimental validation *J. Nucl. Med.* **43** 1031–40 (available at http://jnm.snmjournals.org/content/43/8/1031.short)

Schepis T, Gaemperli O, Treyer V, Valenta I, Burger C, Koepfli P, Namdar M, Adachi I, Alkadhi H and Kaufmann P A 2007 Absolute quantification of myocardial blood flow with 13N-ammonia and 3-dimensional PET *J. Nucl. Med.* **48** 1783–9

Segars W P, Sturgeon G, Mendonca S, Grimes J and Tsui B M 2010 4D XCAT phantom for multimodality imaging research *Med. Phys.* **37** 4902–15

Votaw J R and White M 2001 Comparison of 2-dimensional and 3-dimensional cardiac ^{82}Rb PET studies *J. Nucl. Med.* **42** 701–6 (available at http://jnm.snmjournals.org/content/42/5/701.short)

Watson C C, Casey M E, Eriksson L, Mulnix T, Adams D and Bendriem B 2004 NEMA NU 2 performance tests for scanners with intrinsic radioactivity *J. Nucl. Med.* **45** 822–6 (available at http://jnm.snmjournals.org/content/45/5/822.short)

Watson C C, Newport D and Casey M E 1995 A single scatter simulation technique for scatter correction in 3D PET *Proc. Int. Meeting on Fully Three-Dimensional Image Reconstruction in Radiology and Nuclear Medicine* pp 215–9

Watson C C, Newport D, Casey M E, deKemp R A, Beanlands R S and Schmand M 1997 Evaluation of simulation-based scatter correction for 3-D PET cardiac imaging *IEEE Trans. Nucl. Sci.* **44** 90–97

Yamamoto Y *et al* 1992 A new strategy for the assessment of viable myocardium and regional myocardial blood flow using ^{15}O-water and dynamic positron emission tomography *Circulation* **86** 167–78

Ann Nucl Med (2012) 26:214–221
DOI 10.1007/s12149-011-0561-4

ORIGINAL ARTICLE

Monte Carlo simulation of scintillation photons for the design of a high-resolution SPECT detector dedicated to human brain

Yoshiyuki Hirano · Tsutomu Zeniya · Hidehiro Iida

Received: 15 June 2011 / Accepted: 23 November 2011 / Published online: 13 December 2011

Abstract
Objective In a typical single photon emission computed tomography (SPECT) system, intrinsic spatial resolution depends on the accuracy of the identification of an interacting point, which is dominated by propagation of the scintillation photons in the detector block. This study was intended to establish a Monte Carlo simulation-based evaluation tool taking into account the propagation of scintillation photons to estimate the intrinsic spatial and energy resolutions of the position-sensitive scintillator block in a SPECT detector.
Methods We employed Geant4 Monte Carlo simulation library which incorporated the optical photon processes for two different designs of the position-sensitive scintillator blocks. The validation of the simulation code was performed for a monolithic NaI(Tl) scintillator (251 × 147 × 6.4 mm^3) coupled to 15 flat-panel type multi-anode photo multiplier tubes (PMT) (H8500: Hamamatsu) and results were compared with those obtained experimentally. The code was then applied to a $LaBr_3$(Ce) scintillator of 120 mm square with varied thicknesses for designing high-resolution detector.
Results The simulation resulted in 2.6 mm full width at half maximum (FWHM) of spatial resolution and 9.0% FWHM of energy resolution for the NaI(Tl)-based detector, which were in a good agreement of the experimental results, i.e., 2.7 mm and 10%, respectively. These findings suggest that Geant4 simulation including optical photon processes enables to predict the spatial and energy resolutions of a SPECT detector block accurately. The simulation also demonstrated that 2 mm spatial resolution can be obtained for a 6 mm thickness of the $LaBr_3$(Ce), which is a significant improvement in performance as compared to existing gamma camera system that employs the scintillation detector fitted with PMTs.
Conclusions The Monte Carlo simulation-based evaluation tool was established to estimate the intrinsic spatial and energy resolutions of SPECT detector with position sensitive PMTs. This simulation may be useful to provide an optimal design of a SPECT detector without physical experiments.

Keywords $LaBr_3$(Ce) · Monte Carlo simulation · Geant4 · SPECT · Scintillation photon

Introduction

Single photon emission computed tomography (SPECT) is capable of providing tomographic images of radiolabeled tracers in vivo. The equipment essentially consists of position-sensitive detectors fitted with several types of collimators, which rotate around the object to be imaged. In most SPECT detectors, the point of interaction between a gamma ray and a scintillation crystal is identified by Anger logic on a 2-dimensional domain. Interacting coordinates are calculated by a weighted mean of the deposition of scintillation photons. Spatial resolution depends on the accuracy of identification, which may be degraded as a result of the propagation of scintillation photons within the detector system.

A Monte Carlo simulation is a helpful tool in designing a new detector block. The simulation code is often useful when optimizing design parameters of the detector block,

Y. Hirano (✉) · T. Zeniya · H. Iida
Department of Bio-medical Imaging,
National Cerebral and Cardiovascular Center Research Institute,
5-7-1 Fujishiro-dai, Suita, Osaka 565-8565, Japan
e-mail: hirano@ri.ncvc.go.jp

e.g., the thickness and other geometric parameters of the scintillator as well as the scintillator material, without the need for physical experiments. In order to estimate intrinsic spatial resolution and energy resolution, it is essential to understand the process of transport of scintillation photons in the detector system, as well as the interaction of gamma rays with materials. Geant4 [1] makes it possible to simulate both these processes. Simulation studies on propagation of scintillation photons have been performed using Geant4 (or other code) [2–6]. However, it is difficult to reproduce the intrinsic spatial and energy resolutions accurately due to the many unknown factors (e.g., optical properties of materials and electrical noise) to simulate transporting scintillation photons. Resolutions essentially depend on the number of obtained scintillation photons. Geant4 does not include the optical properties of materials, such as absorption length, refraction index, and reflection. These data must be entered into Gean4 by users. The simulation accuracy is sensitive to these optical parameters. To our knowledge, a validation study on spatial and energy resolutions using Geant4 was performed only by Van Der Laan et al. [2] for a positron emission tomography (PET) instrument that employed a monolithic scintillators (LYSO(Ce): $20 \times 10 \times 10$ mm^3 and $20 \times 10 \times 20$ mm^3) and avalanche photodiodes (APD).

In this work, we intended to use Geant4 for two types of position-sensitive scintillation detector in a SPECT system. Both detectors consist of a monolithic scintillator and flat-panel type multi-anode PMTs (H8500: Hamamatsu). These are different from detectors used in previous study [2] regarding scintillator material, detector size and photo-sensors. With regard to photo-sensor, detection principle of PMT is absolutely different from that of APD. One detector has a larger field-of-view (FOV) and is fitted with a parallel beam collimator for imaging the whole human brain. The detector block consists of a NaI(Tl) scintillator ($251 \times 147 \times 6.4$ mm^3) and 15 PMTs. Its experimental physical performance was used to validate the simulation code, including the photon propagation processes. We then extended this simulation geometry to another detector block, which consists of a $LaBr_3$(Ce) scintillator [7, 8] coupled to 4 PMTs to achieve higher intrinsic spatial resolution. This detector has smaller FOV and may be fitted with a pinhole collimator for focused imaging of a limited area of the brain with higher spatial resolution of approximately 1 mm [9]. We also investigated effects of inclined incident angle of gamma rays into the detector in a pinhole configuration on spatial resolution of the detector system.

Materials and methods

Monte Carlo simulation

We employed the Monte Carlo simulation library Geant4 (version 9.2.p02) in this study. Geant4 enables us to simulate not only interaction of gamma rays with several materials but also transport of scintillation photons. In this simulation, we took into account the following electromagnetic processes: Compton scatter, photo-electric effect, Rayleigh scatter, multiple scatter, bremsstrahlung, and ionization. The first three processes involve gamma rays; the rest involve electrons. Optical photon processes in the propagation of scintillation photons were also included: absorption, Rayleigh scatter, reflection, and refraction.

Simulations were carried out for essentially two sets of detector configurations as follows. The two sets of detector configurations (large-FOV detector and small-FOV detector) were precisely reproduced as shown in Fig. 1. The simulation configurations included scintillator, reflector, optical window, optical grease, PMT window, and PMT cathodes. Gamma rays entered the detector vertically,

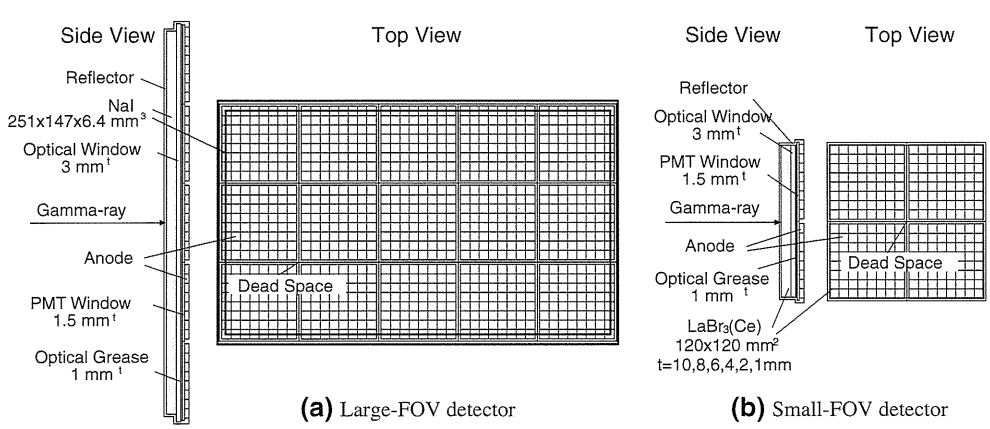

Fig. 1 Geometrical configurations of the large-FOV detector (**a**) and the small-FOV detector (**b**). In the simulation, we included the scintillator, reflector, optical window, optical grease, PMT window, and PMT anodes. The scintillator thickness of the small-FOV detector was varied (10, 8, 6, 4, 2, and 1 mm)

except for the simulation carried out for a pinhole configuration. When a gamma ray interacted with the scintillator and deposited its energy, scintillation photons were emitted isotropically. The emission spectra of NaI(Tl) and $LaBr_3$(Ce) are shown in Fig. 2a. The number of scintillation photons followed the Poisson distribution, and the mean was proportional to the energy deposition ($LaBr_3$(Ce): 63 photons/keV; NaI(Tl): 38 photons/keV). The scintillation photons propagated in the scintillator, optical window, optical grease and PMT window. At the reflector, the Lambert reflection was applied. The reflectance was 0.95 (white plastic). For a photon that was not reflected, propagation was terminated. At other boundaries between materials, the Fresnel reflection or Fresnel refraction was applied. When scintillation photon reached a cathode, the detection was determined by the quantum efficiency (Fig. 2a, gray line) and the collection efficiency (60%) of the H8500. The interacting point was reconstructed by Anger logic. An error of 17% was assigned to the anode gain. The error was estimated from anode uniformity map described in the specification. Transmittances of NaI(Tl) and borosilicate glass are shown in Fig. 2b. PMT cathodes and dead space surrounding the cathodes were assumed to be perfect absorbers. This simulation did not include absorptions by $LaBr_3$(Ce) and optical grease, because these transmittance data are not available. However, according to [10], the absorption for visible light is low. The thickness of optical grease was assumed as 1 mm. Refractive indices of, NaI(Tl), $LaBr_3$(Ce) and optical grease are 1.85, 1.9 and 1.465, respectively. With regard to borosilicate glass, the index was shown in Fig. 2c. These data were obtained from each specification.

Validation of the simulation code

To validate the Monte Carlo simulation, we compared spatial and energy resolutions obtained from the simulation with experimental values for the large-FOV detector. The experimental setup was as follows. The detector consisted of a monolithic NaI(Tl) scintillator (Saint-gobain) of $251 \times 147 \times 6.4$ mm^3, fitted to 15 flat-panel type multi-anode PMTs (H8500: Hamamatsu) arranged in a 5×3 array. Each of the PMTs had 64 cathodes (8×8 array) that measured 5.8 mm square (6.08 mm pitch at center). The size of each PMT was 52×52 mm^2, and the PMT window was a 1.5 mm thickness of borosilicate glass that was transparent to visible lights. The NaI(Tl) scintillator was covered with a white diffuse reflector and an optical window of 3 mm thickness at the connection side of the PMTs. The optical window was also made of borosilicate glass. The NaI(Tl) scintillator was coupled to the PMTs by optical grease (BC630: Saint-gobain). Electric resistance arrays were connected to the anode outputs. The sum of the anode outputs and the positional coordinate (x, y) calculated by Anger logic were recorded in list mode. A specially designed collimator was placed in front of the detector block. The collimator was a $300 \times 200 \times 10$ mm^3 block of lead with 170 holes of 1.5 mm diameter arranged in a 17×10 grid pattern with a grid interval of 15 mm. Small-tube sources (7 mm diameter) filled with Tc-99m solution were placed on 170 collimator holes, and position dependency of the energy spectra and point spread functions were measured. Energy and spatial resolutions were then evaluated.

In the simulation, spatial and energy resolutions were evaluated for the NaI(Tl)-based large-FOV detector by exposing 3000 gamma rays (141 keV) to the detector as a parallel beam with a circular distribution of 1.5 mm diameter at each of the hole positions. Interactions with the collimator were not included to reduce the computing time.

Application to the design of a new detector

Another series of simulations were carried out for the small-FOV detector to optimize the geometrical parameters. The scintillator was assumed to be $LaBr_3$(Ce) with a surface area of 120×120 mm^2. The scintillator was coupled to 4 PMTs (H8500) arranged in a 2×2 array. The

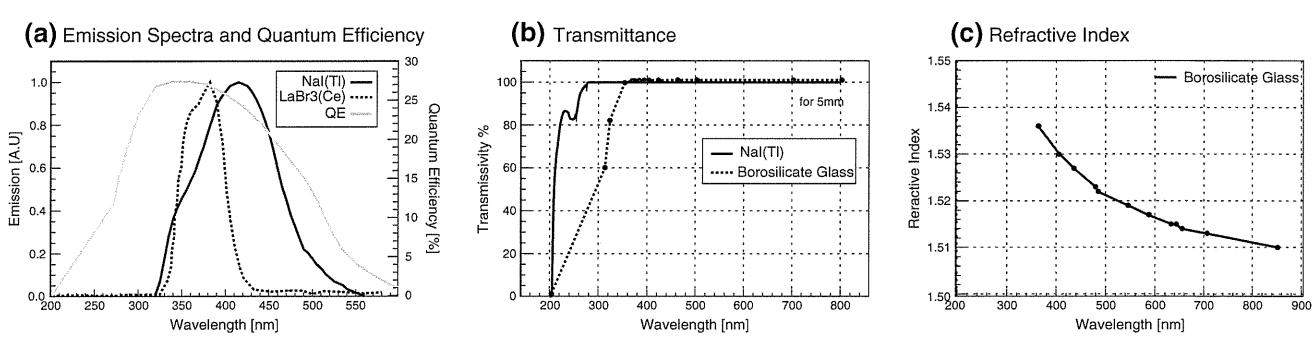

Fig. 2 **a** Emission spectra of NaI(Tl) (*solid line*) and $LaBr_3$(Ce) (*dotted line*) (BrilLanCe350: Saint-gobain) together with the quantum efficiency of the H8500 (*gray line*). **b** Transmittance of NaI(Tl) and borosilicate glass (assumed BK7: Schott Glass). **c** Refractive index of borosilicate glass. These data are available from each specification

surface of the scintillator was covered with a white diffuse reflector. The thickness of the scintillator was varied (10, 8, 6, 4, 2, and 1 mm) and the optical window thickness was also varied (1 and 3 mm). Simulation was also carried out using NaI(Tl) instead of $LaBr_3$(Ce) as the reference. Additional simulations were performed to evaluate effects of varying incident angle for a detector fitted with a pinhole collimator. Finally, detection efficiency defined as follows was estimated

$$\text{Efficency} = \frac{\text{Number of full energy despitions}}{\text{Number of incident gamma rays}}.$$

Densities of NaI(Tl) and $LaBr_3$(Ce) were 3.67 and 5.08 g/cm^3, respectively.

Gamma rays (141 keV) entered the scintillator vertically at 49 positions on a 7 × 7 grid with 15 mm intervals, similar to the source position of the large-FOV detector. In the pinhole configuration, gamma rays were generated at a point 86.6 mm above the center of the detector to the 49 positions. The maximum incident angle was 60°. 1000 gamma rays were simulated at each position.

Analysis

In both the simulation and experiment, the spatial and energy resolutions were evaluated at every grid points as follows. Photo-peak of 141 keV was fitted using a Gauss function, and 3-sigma region as an energy window (e.g., 116–164 keV for the experiment with NaI(Tl)) was selected. Using energy-selected events, interacting points were reconstructed by Anger logic and projected into the x and y directions. The spatial resolution was calculated by fitting with a function that took into account the diameter of holes, expressed as follows:

$$f(x) = \int g(x) \times h(z-x)\mathrm{d}x = \frac{1}{2a}\left\{\mathrm{erf}\left(\frac{a+b-x}{\sqrt{2}\sigma}\right) - \mathrm{erf}\left(\frac{b-x}{\sqrt{2}\sigma}\right)\right\},$$

$f(x)$ is assumed to be a convolution function of the Gauss function $g(x)$, which serves as a point spread function, and the uniform distribution $h(x)$, which describes the source distribution. erf is an error function, a is the diameter of a hole, and b is the position of a hole. The spatial resolutions for each position were calculated according to the term $\sqrt{8\ln 2} \times \sigma$, where σ is the standard deviation of the Gauss function. Finally, the energy resolution was derived from the energy spectra at each position. In this analysis of the experiment, background counts were subtracted from the experimental data.

We compared spatial resolution (FWHM mm) and energy resolution (FWHM %) with experimental results of the large-FOV detector. The planar image, spatial resolution in x and y direction, energy spectra, and their average resolutions were used for the comparisons. Finally, the small-FOV detector was designed to optimize spatial resolution and detection efficiency.

Results

Validation of simulation code

Planar images of multiple point sources obtained from the experiment and the simulation for the large-FOV detector are shown in Fig. 3. It can be seen that intervals between points are constant around the center, but becomes closer at the edge. The spatial resolution in the x direction along the central line is shown in Fig. 4. The spatial resolutions are almost homogenous around the center but become gradually worse at the edge of the detector in both the simulation and experiment. In the simulation, spatial resolution agreed with the experimental results within approximately 10% at ± 105 mm distance from the center. At the position 10 mm away from the detector edge, the resolutions become relatively worse. The experimental mean resolution, omitting those from the edge, were 3.6 and 3.1 mm in

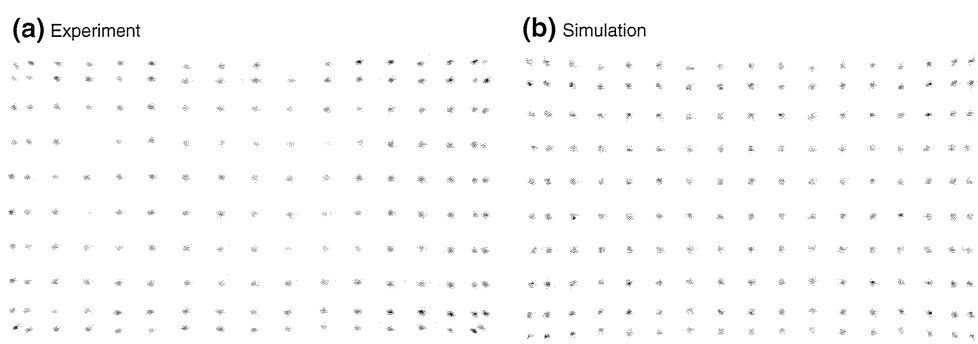

Fig. 3 Planar images of multiple point sources obtained from experiment (**a**) and simulation (**b**). These interacting points are calculated by Anger logic

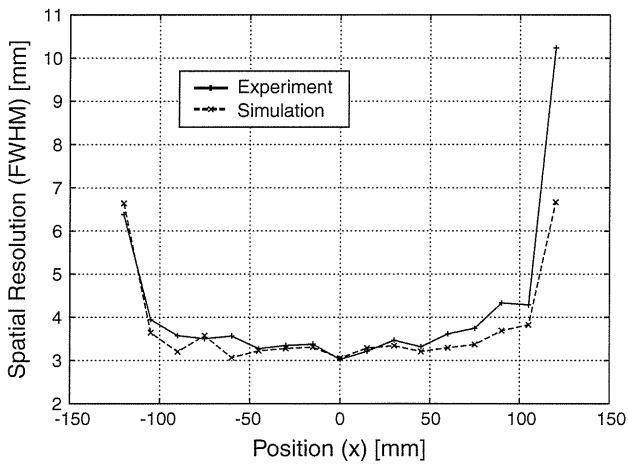

Fig. 4 Comparison of spatial resolutions in the x direction. The resolutions are for lines from the 5th row from the bottom in Fig. 3. The *solid line* shows the experimental result, and the *dotted line* shows the simulation result

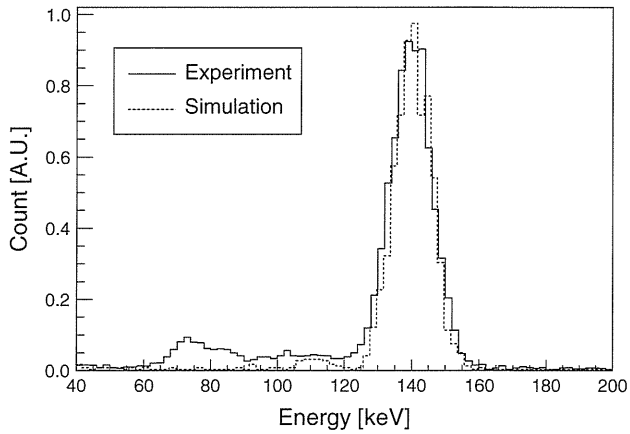

Fig. 5 Energy spectra at the center of the detector. The *solid line* shows experimental results; the *dotted line* shows the simulation. In the simulation, energy spectra are derived from the number of obtained scintillation photons

the x and y directions, respectively. The best resolutions in the x and y directions were 3.0 and 2.7 mm; these were obtained at the center. In the simulation, the mean resolutions in the x and y directions were 3.3 and 3.0 mm, respectively. The best resolutions were 2.8 and 2.6 mm for the x and y directions. Figure 5 shows the energy spectra at the center. The broadness of the peak in the simulation corresponds to the fluctuation of the number of obtained scintillation photons. The energy resolutions determined from spectra of the experiment and the simulation were 10.0 and 9.0% (FWHM), respectively. With respect to energy resolution, clear position dependence was not observed. The mean and deviation of energy resolution of the experiment and the simulation, respectively, were 10.3 ± 0.2 and 9.3 ± 0.3%.

Application of the simulation code for designing high-resolution detector

The simulation results of planar images of multiple point sources for the small-FOV detector with different thicknesses (10, 6 and 1 mm) are shown in Fig. 6. Clear separation of source positions was obtained in the thin scintillator, especially the 1 mm thickness. As the scintillator was thicker, interval of source positions decreased and the point spread function blurred. The mean spatial resolutions with thicknesses of 10, 8, 6, 4, 2, and 1 mm are shown in Fig. 7a together with the cases in which the scintillator is NaI(Tl), the thickness of the optical window is 1 or 3 mm, and the angle of incidence is oblique. In these configurations, comparable resolutions in the x and y directions were obtained. $LaBr_3$(Ce) had better spatial resolution than NaI(Tl) by 22–36%. The best resolution was 0.76 mm with 1 mm thickness. Energy spectra obtained from $LaBr_3$(Ce) and NaI(Tl) of 1 mm thickness at the center of the detector were shown in Fig. 8. The numbers of obtained scintillation photons in an event of full energy deposition (141 keV) were 5039 and 3103, resulting in energy resolution of 8.65 and 11.7%, respectively. The detection efficiencies are shown in Fig. 7b. The maximum efficiency for the 141 keV gamma rays was 93% with 10 mm thickness. The efficiency decreased with thinner scintillator (26% for 1 mm thickness). Varying the optical window between 1 and 3 mm had little effect. For the oblique incident cases, the spatial resolution became slightly worse by several percent.

Figure 9 shows an average distribution of scintillation photons on the 16 × 16 anodes in the case of 1000 gamma rays entering the of the detector. The thicker scintillator has a wider spread of scintillation photons.

Discussion

Adequacy of the simulation

This study demonstrates the adequacy of the simulation code. Both the spatial resolution and the energy resolution appeared to be well reproduced between simulation and experimental data. It has thus been suggested that Geant4 with optical photon processes would be of use when one intends to optimize the design of a new scintillation detector assembly. However, the simulation systematically exhibited small but significant overestimations compared with the experimental data. This can probably be attributed to additional errors in the experiments, which have not been taken into account in the simulation. Potentially influential factors include electrical noise and/or uncertainties in the multiplying processes of the PMTs. The angular

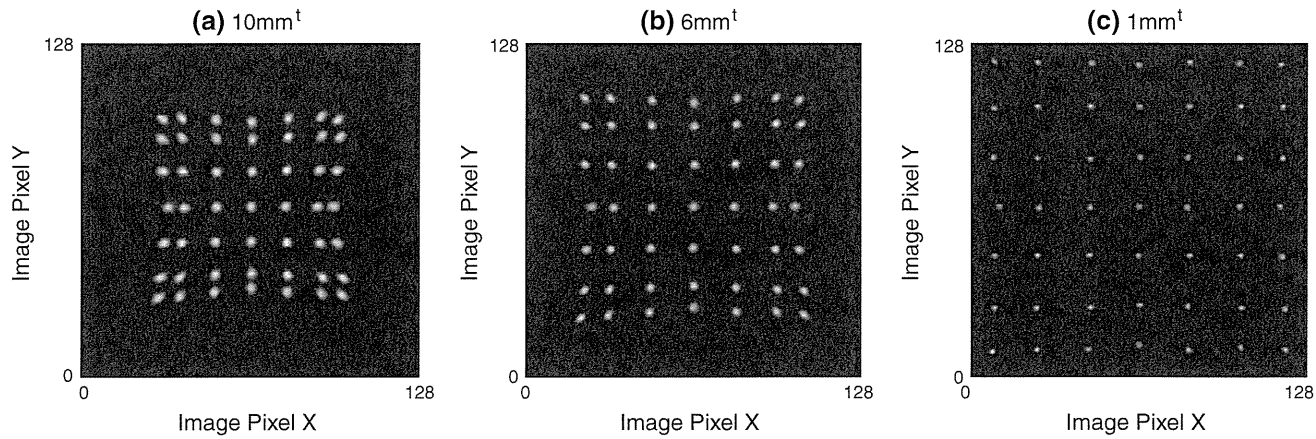

Fig. 6 Reconstruction of interacting points with a simulated $LaBr_3(Ce)$ scintillator with thickness 10 mm (**a**), 6 mm (**b**), or 1 mm (**c**). 141 keV gamma rays entered the $LaBr_3(Ce)$ scintillator vertically at 49 positions arranged in a 7 × 7 grid pattern with 15 mm intervals. Thinner scintillators have better spatial resolutions. Good separations and position linearity were obtained with a 1-mm thickness

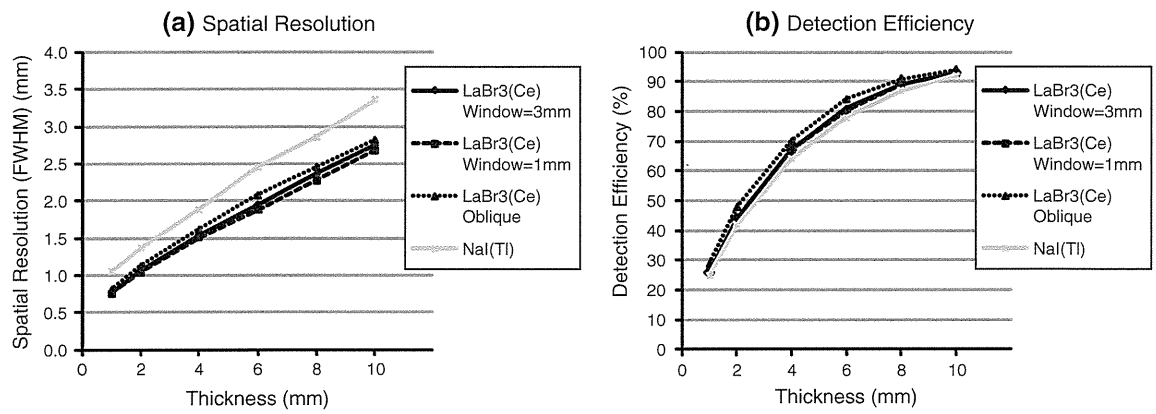

Fig. 7 Spatial resolutions (FWHM, mm) and detection efficiency (%) of the small-FOV detector estimated by simulation. Thickness was varied from 10 to 1 mm."OpWin" stands for the optical window. "Oblique" means that gamma rays enter the scintillator at an oblique angle

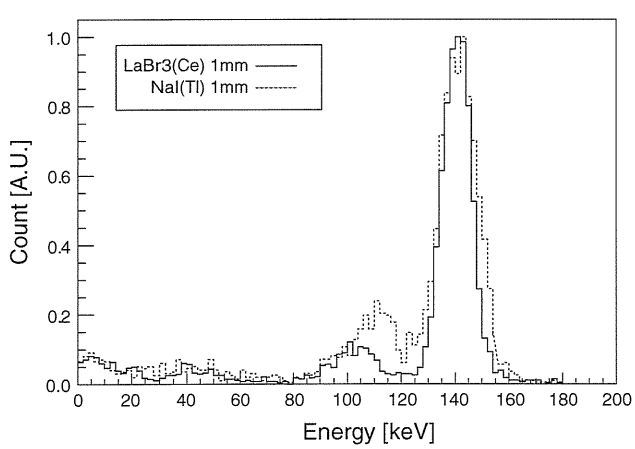

Fig. 8 Energy spectra $LaBr_3(Ce)$ (*solid line*) and NaI(Tl) (*dot line*) of 1 mm thickness at the center of the small FOV detector normalized by the maximum counts. Energy resolutions of $LaBr_3(Ce)$ and NaI(Tl) were 8.65 and 11.7%, respectively

distribution of the source is also considered as an influential factor. The beam was parallel in the simulation, but there were slight obliquely incidents in the experiment. Differences in the spatial resolution in the x and y directions can be attributed to difference of the number of cathodes along the x and y axes. The larger number of cathodes causes a larger uncertainty in the position identification due to the statistical fluctuation of scintillation photons at each anode. Note that the simulation of a square detector geometry for the small-FOV detector resulted in comparable resolutions for both the x and y directions. The spatial resolution has a position dependency, and decreases near the edge. This is because the distribution of the scintillation photons entering the cathodes is isotropic at the center, while scintillation photons partially reflect at the edge, resulting in an asymmetrical distribution at the edge of the detector. This caused decreased linearity performance and degraded spatial

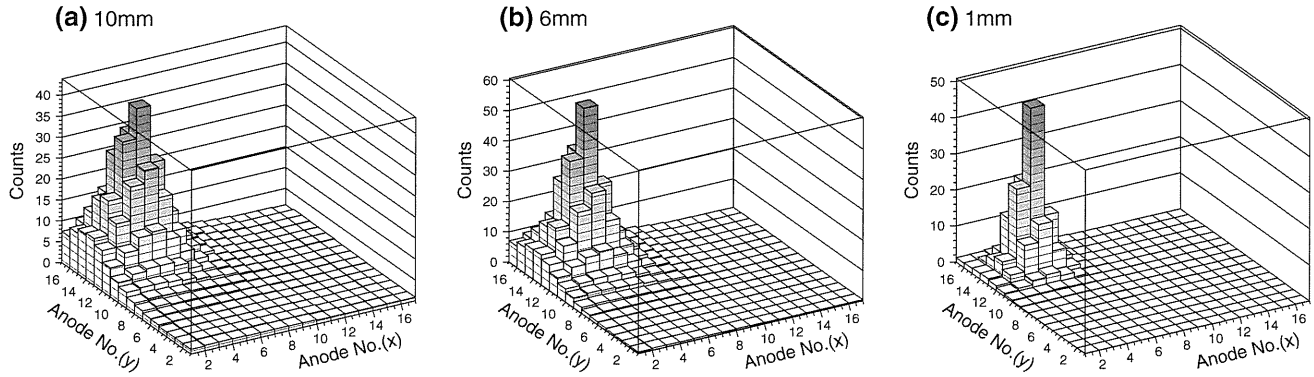

Fig. 9 Average distribution of scintillation photons on the 16 × 16 array of anodes. Gamma rays enter the edge of the detector. Scintillator thickness is 10 mm (**a**), 6 mm (**b**), or 1 mm (**c**)

resolution near the edge. Energy resolution depends on the number of observed scintillation photons. Homogeneous energy resolution indicates that the correction efficiencies of scintillation photons are almost equal over the entire detector. Importantly, the energy resolution was highly reproducible without any arbitrary parameters. It is often the case in most Monte Carlo simulation studies that energy resolution is fitted to match the experimental results. However, this simulation can reproduce the energy resolutions for a given set of detector design parameters. This is one of the most important features of this study. The simulated energy spectrum of the scatter region (below 120 keV) was different from the experimental results. It was probably due to the scatter from the collimator in the experiment. The simulation did not include interaction with the collimator.

Conceptual design of high-resolution SPECT system for human brain

We performed the simulation for optimizing a new high-resolution detector system for SPECT described in [9]. A pinhole collimator can be adopted to achieve the high spatial resolution typically achieved with a small-FOV. The reconstructed FOV can, however, be truncated if applied to an object which is larger than the FOV; this truncation can cause artifacts in the reconstructed images, and errors in the quantitative pixel counts. A new technique for truncation-compensated 3D-OSEM reconstruction [11], based on the theory proposed by Kudo et al. [12], could be one application of the two detectors presented in this study. One detector, with an NaI(Tl)-based large-FOV detector, provides an image without truncation, and is used as a supporting information for reconstructing truncated data from the small-FOV detector successfully. The small-FOV detector has the potential to provide high resolution of approximately 1 mm, but with possible truncation. Thus, the combination of the two types of detectors may provide SPECT images with both high spatial resolution and the quantitative accuracy of a magnified FOV. To achieve such a high resolution in practice, a prior high-accuracy estimate is essential. Monte Carlo simulation code, validated for a scintillator based on multi-anode PMTs, would be helpful for optimizing and validating various design configurations.

Design of the small-FOV detector with high resolution

$LaBr_3(Ce)$ is a promising material for use in scintillator crystals to achieve higher resolution than NaI(Tl); this is primarily due to the larger amount of scintillation photons, as demonstrated in this study. The thinner scintillator provides better spatial resolution, because thinner scintillators prevent the spread of scintillation photons, as shown in Figs. 6, 7 and 9. However, efficiency decreases with a thinner scintillator crystal, resulting in reduced sensitivity of gamma-ray detection. Thus, there is a trade-off between spatial resolution and detection efficiency. A thickness of 6 mm appeared to be best suited for our detector system, as we originally aimed at achieving a spatial resolution ~1 mm with sufficient detection efficiency. If we use a pinhole collimator with 0.5 mm diameter and threefold magnification factor, an intrinsic spatial resolution of ~2 mm would provide the spatial resolution of 1 mm in a SPECT system [13]. The simulation demonstrated that a 6 mm thickness of $LaBr_3(Ce)$ can provide ~2 mm intrinsic spatial resolution and a detection efficiency of approximately 86% for Tc-99m, that efficiency is comparable to the performance of currently popular SPECT detectors. Using a pinhole collimator, spatial resolution could be slightly worse; this would be attributed to the spread of interaction points in the x–y plane due to the oblique angle of incidence. To evaluate the differences between vertical and oblique angles of incidence, it is necessary to simulate both gamma rays and scintillation photons, as we have done in this simulation study. Geant4 is of use for such evaluations, because it takes both processes into account.

Detector systems that consist of a monolithic scintillator and multi-anode PMTs have the potential to improve spatial resolution over what is currently achievable. In this study, Anger logic using all anodes was employed to identify an interacting point. Anger logic using a subset of anodes will improve the spatial resolution, the nearest-neighbor algorithm [14], and nonlinear least squares method [15] are also promising methods. In the future, in order to employ these methods, analog-to-digital converters (ADC) for all anodes will be installed in our detector systems.

Conclusion

We performed the Geant4 simulation that took into account propagation of gamma rays and transport of scintillation photons. The simulation reproduced experimental results with regard to both spatial resolution and energy resolution for a SPECT detector based on NaI(Tl) scintillator and position sensitive PMTs (H8500). We demonstrated a simulation for a design of the small-FOV detector to optimize geometrical parameter. This simulation may be useful to provide an optimal design of a SPECT detector without physical experiments.

Acknowledgments The authors would like to thank Mr. Hiroyuki Mashino of EspecTecno Corporation, Kobe, Japan, for his skillful assistance with an acquisition system of the detector. This work was supported in part by the Project from Kansai Bureau of Economy, Trade and Industry of Japan; a Grant for Research on Health Labour Sciences Research Grant, from the Ministry of Health, Labour and Welfare (MHLW) of Japan; the Budget for Nuclear Research of the Ministry of Education, Culture, Sports, Science and Technology (MEXT) of Japan; and the Grant-in-Aid for Scientific Research from MEXT of Japan.

References

1. Agostinelli S, Allison J, Amako K, Apostolakis J, Araujo H, Arce P, et al. GEANT4 a simulation toolkit. Nucl Instrum Methods Phys Res A. 2003;506:250–303.
2. Van Der Laan DJ, Dennis RS, Maas MC, Beekman FJ, Bruyndonckx P, van Eijk CWE. Optical simulation of monolithic scintillator detectors using GATE/GEANT4. Phys Med Biol. 2010;55:1659–75.
3. Sergio LM, Giuseppe B, Paolo B, Dante B, Valentino OC, et al. Optical physics of scintillation imagers by GEANT4 simulations. Nucl Instrum Methods Phys Res A. 2009;607:259–60.
4. Ciocia F, Braem A, Chesi E, Leo RD, Joram C, Lagamba L, et al. GEANT4 studies on the propagation and detection of scintillation light in long thin YAP crystals. Nucl Instrum Methods Phys Res A. 3009;600:506–12.
5. Wirth S, Metzger W, Pham-Gia K, Heismann BJ. Impact of photon transport properties on the detection efficiency of scintillator arrays. IEEE Nuclear Sci Symp Confer Record. 2006; 2602–3
6. Soreefan AM, Hui T, DeVol TA, Dept. Experimental and monte carlo investigation of the light collection efficiency of heterogenous scintillation flow cell detectors. IEEE Nuclear Sci Symp Confer Record. 2003;760–2
7. Pani R, Pellegrini R, Cinti MN, Bennatia P, Bettia M, Vittorinia F, et al. LaBr3:Ce crystal: the latest advance for scintillation cameras. Nucl Instrum Methods Phys Res A. 2007;572:268–9.
8. Pani R, Cinti MN, Pellegrinia R, Bennatia P, Bettia M, Vittorinia F, et al. LaBr3:Ce scintillation gamma camera prototype for X and gamma ray imaging. Nucl Instrum Methods Phys Res A. 2007;576:15–8.
9. Zeniya T, Hirano Y, Sakimoto T, Ishida K, Watabe H, Teramoto T, et al. Conceptual design of high resolution and a quantitative SPECT system for imaging a selected small ROI of human brain. IEEE Nuclear Sci Symp Confer Record. 2009; 3484–6
10. Li C, Wang B, Wang R, Wang H, Zhu Z. First-principles study of the electronic and optical properties of lanthanide bromide. Thin Solid Films. 2008;516:7894–8.
11. Zeniya T, Watabe H, Inomata T, Iida H, A Sohlberg, H Kudo. 3DOSEM reconstruction from truncated data in pinhole SPECT. IEEE Nuclear Sci Symp Confer Record. 2007; 4205–7
12. Kudo H, Courdurier M, Noo F, Defrise M. Tiny a prior knowledge solves the interior problem in computed tomography. Phys Med Biol. 2008;53:2207–31.
13. Jaszczak RJ, Li J, Wang H, Zalutsky MR, Coleman RE. Pinhole collimation for ultra-high-resolution small-field-of-view SPECT. Phys Med Biol. 1994;39:425–37.
14. Maas MC, Schaart DR, Van Der Laan DJ, Bruyndonckx P, Lemaitre C, Beekman FJ, et al. Monolithic scintillator PET detectors with intrinsic depth-of-interaction correction. Phys Med Biol. 2009;54:1893–908.
15. Zhi Li, Wedrowski M, Bruyndonckx P, Vandersteen G. Nonlinear least-squares modeling of 3D interaction position in a monolithic scintillator block. Phys Med Biol. 2010;55:6515–32.

IOP PUBLISHING PHYSICS IN MEDICINE AND BIOLOGY

Phys. Med. Biol. **57** (2012) 7873–7892 doi:10.1088/0031-9155/57/23/7873

Quantitative assessment of regional cerebral blood flow by dynamic susceptibility contrast-enhanced MRI, without the need for arterial blood signals

Jun-ichiro Enmi[1], Nobuyuki Kudomi[2], Takuya Hayashi[3], Akihide Yamamoto[1], Satoshi Iguchi[1], Tetsuaki Moriguchi[1], Yuki Hori[1], Kazuhiro Koshino[1], Tsutomu Zeniya[1], Nadim Jon Shah[4,5], Naoaki Yamada[6] and Hidehiro Iida[1]

[1] Department of Investigative Radiology, National Cerebral and Cardiovascular Center Research Institute, 5-7-1 Fujishiro-dai, Suita City, Osaka 565-8565, Japan
[2] Department of Medical Physics, Faculty of Medicine, Kagawa University, Ikenobe 1750-1, Miki-cho, Kita-gun, Kagawa, 761-0793, Japan
[3] Functional Probe Research Laboratory, RIKEN Center for Molecular Imaging Science, 6-7-3 Minatojima-minamimachi, Chuo-ku, Kobe, Hyogo, 650-0047, Japan
[4] Institute of Neuroscience and Medicine-4, Medical Imaging Physics, Forschungszentrum Jülich GmbH, 52425 Jülich, Germany
[5] Department of Neurology, Faculty of Medicine, JARA, RWTH Aachen University, 52074 Aachen, Germany
[6] Department of Radiology, National Cerebral and Cardiovascular Center, 5-7-1 Fujishiro-dai, Suita City, Osaka 565-8565, Japan

E-mail: enmi.junichiro.ri@mail.ncvc.go.jp

Received 18 December 2011, in final form 2 September 2012
Published 14 November 2012
Online at stacks.iop.org/PMB/57/7873

Abstract

In dynamic susceptibility contrast-enhanced magnetic resonance imaging (DSC-MRI), an arterial input function (AIF) is usually obtained from a time–concentration curve (TCC) of the cerebral artery. This study was aimed at developing an alternative technique for reconstructing AIF from TCCs of multiple brain regions. AIF was formulated by a multi-exponential function using four parameters, and the parameters were determined so that the AIF curves convolved with a model of tissue response reproduced the measured TCCs for 20 regions. Systematic simulations were performed to evaluate the effects of possible error sources. DSC-MRI and positron emission tomography (PET) studies were performed on 14 patients with major cerebral artery occlusion. Cerebral blood flow (CBF) images were calculated from DSC-MRI data, using our novel method alongside conventional AIF estimations, and compared with those from ^{15}O-PET. Simulations showed that the calculated CBF values were sensitive to variations in the assumptions regarding cerebral blood volume. Nevertheless, AIFs were reasonably reconstructed for all patients. The difference in CBF values between DSC-MRI and PET was -2.2 ± 7.4 ml/100 g/min ($r = 0.55$, $p < 0.01$) for our method, versus -0.2 ± 8.2 ml/100 g/min ($r = 0.47$, $p = 0.01$) for the conventional method.

0031-9155/12/237873+20$33.00 Printed in the UK & the USA 7873

The difference in the ratio of affected to unaffected hemispheres between DSC-MRI and PET was 0.07 ± 0.09 ($r = 0.82$, $p < 0.01$) for our method, versus 0.07 ± 0.09 ($r = 0.83$, $p < 0.01$) for the conventional method. The contrasts in CBF images from our method were the same as those from the conventional method. These findings suggest the feasibility of assessing CBF without arterial blood signals.

(Some figures may appear in colour only in the online journal)

1. Introduction

Quantitation of cerebral blood flow (CBF) provides essential information about pathophysiological status in cerebral ischemic disease. Dynamic susceptibility contrast-enhanced magnetic resonance imaging (DSC-MRI) has been extensively utilized to assess quantitative or semi-quantitative CBF images in clinical settings (Calamante *et al* 1999). The most commonly accepted technique for quantitation is based on the deconvolution of the time–concentration curve (TCC) of cerebral tissues using the arterial input function (AIF), as originally proposed by Østergaard and co-workers (Østergaard *et al* 1996a, 1996b).

In general, AIF is required in quantitative assessment of perfusion in cerebral and other tissue. In the field of nuclear medicine, the standard technique for obtaining AIF is based on the arterial blood sampling. The arterial-blood-sampling-based technique has also been applied to quantitative assessment of perfusion using MRI with gadopentetate dimeglumine (Gd-DTPA) (Larsson *et al* 1990, Fritz-Hansen *et al* 1996), but is invasive and requires labor intensive works. Thus, AIF has normally been obtained from the arterial blood signals obtained from MR images by selecting regions of interest (ROIs) on a pertinent artery, e.g., the internal carotid artery (ICA), middle cerebral artery (MCA) (Calamante *et al* 1999), or aorta (Brix *et al* 2004). Such a technique (the arterial voxel selection method) however suffers from errors attributed to the cross contamination between the artery and adjacent tissue or the partial volume effect (van Osch *et al* 2001, Hansen *et al* 2009). It is also important to note that the nonlinear relationship exists between the tracer concentration and the relaxation rate (van Osch *et al* 2003), causing systematic errors in AIF thus in CBF.

Recently, an alternative technique has been developed by Yang *et al* (2004, 2007) and Schabel *et al* (2010a, 2010b), with the intention of reducing the effects to the partial volume effect, and minimizing errors caused by the nonlinear relationship between contrast agent concentrations and relaxation time. In such techniques, AIF was reconstructed from tissue TCCs; thus errors attributed to the partial volume effect could be reduced. An additional advantage of this approach is the reduced dynamic range of MR signals. Recently, our group proposed a technique to reconstruct AIF from tissue time–activity curves (TTACs) in PET, based on a mathematical formulation that describes the AIF with only a small number of parameters (Kudomi *et al* 2008). The parameters were determined so that TTACs in multiple tissue regions simulated by the convolution of the AIF by tissue-response functions reproduced the observed TTAC best by means of the nonlinear least-squares minimization procedures. This study demonstrated that the AIF could be accurately reproduced from a sequential PET image obtained with i.v. ^{15}O-water, enabling the quantitative assessment of regional hepatic blood flow images in clinical settings.

In this study, we extended the tissue-based method of Kudomi *et al* (2008) to the quantitatively assessment of CBF in the DSC-MRI. Verification of this method was first evaluated by systematic simulations, and then validated in patient population, by referring the PET technique as a gold standard.

2. Materials and methods

2.1. Theory

To reconstruct AIF from TCCs of multiple brain regions, a model function was assumed for AIF:

$$C_{\text{Artery}}(t) = \begin{cases} 0 & (t < t_1) \\ \frac{A}{K_e^2(1+\alpha)^2}[1 - \exp\{K_e(1+\alpha)(t_1 - t)\}] & (t_1 \leqslant t \leqslant t_2) \\ \frac{A}{K_e^2(1+\alpha)^2}[\exp\{K_e(1+\alpha)(t_1 - t_2)\} + \exp\{K_e(1+\alpha)(\mathrm{t}_2 - \mathrm{t})\} \\ \quad -2 \cdot \exp\{K_e(1+\alpha)(t_1 - t)\}] & (t > t_2) \end{cases} \quad (1)$$

where the model function was derived by assuming that the contrast agent is intravenously administered between t_1 and t_2 at a constant rate of A, and that the agent diffuses back and forth between arterial blood and whole-body interstitial spaces at rates αK_e and K_e, respectively (Kudomi *et al* 2008) (see figure 1(a)). The TCC of cerebral tissue ($C_{\text{Tissue}}(t)$) in a given volume segment was expressed as

$$C_{\text{Tissue}}(t) = f \cdot C_{\text{Artery}}(t) \otimes \mathrm{e}^{-\frac{f}{v}t}, \quad (2)$$

where f and v are CBF and cerebral blood volume (CBV) in the volume segment, respectively. The residue function was assumed to follow a single-compartment model that could be expressed by a single-exponential function, consistent with an approach frequently used in previous simulation studies (Calamante *et al* 2000, 2007, Wu *et al* 2003a, Smith *et al* 2004, Salluzzi *et al* 2005, Willats *et al* 2006). TCCs of tissues were obtained from different brain regions of normal gray matter, and used in the AIF reconstruction as follows, as previously described (Kudomi *et al* 2008).

In addition to f for each region, four parameters describing the shape of the AIF (A, $K_e(1+\alpha)$, t_1 and t_2-t_1) were determined by means of the combination of nonlinear least-squares and grid search minimization, such that the TCCs of multiple brain regions were best fit to (2), as illustrated in figure 1(b). Detailed procedures are essentially the same as in the previous report (Kudomi *et al* 2008). Three important assumptions were made as follows. (1) There is a single AIF common over all brain regions, and therefore one set of the four parameters can be shared among all the tissues selected for reconstructing AIF; (2) while f varies among regions, CBV is assumed to have a constant value of 4 ml/100 g, a typical value for a normal gray-matter region (Yamaguchi *et al* 1986, Ito *et al* 2004); and (3) there is no difference in the tracer arrival time among different tissue regions. The second assumption is intended to provide a unique absolute scale (A), which corresponds to the height of AIF. If this assumption is absent, then only relative A, and hence relative f, can be determined. The AIF was computed by substituting the obtained parameter values into (1). CBF images were calculated by deconvolving the TCC of each voxel in dynamic MRI images with the reconstructed AIF.

2.2. Simulation study

Systematic simulations were carried out in order to evaluate the effects of possible errors on the reconstructed AIFs and resultant CBF values. The first simulation was carried out in order to evaluate the effect of the estimation error of each parameter describing the shape of the model function on resultant CBF value. In the second simulation, the effect of finite sampling period on the shape of reconstructed AIF and resultant CBF was evaluated. The third simulation was